

Theoretical Characteristics of a Three-Point Roberts Linkage

M. Otsuka,^{1,2} K. Mitsuhashi,^{1,2} R. Takahashi,^{2,3} Y. Nishino,^{1,2} Y. Aso,^{2,3} and T. Tomaru^{1,2,3}

¹⁾Graduate School of Science, the University of Tokyo, 7-3-1 Hongō, Bunkyo, Tokyo, 113-0033 Japan

²⁾National Astronomical Observatory of Japan, 2-21-1 Osawa, Mitaka, Tokyo, 181-0015 Japan

³⁾The Graduate University for Advanced Studies, SOKENDAI, Shonan Village, Hayama, Kanagawa, 240-0193 Japan

(*Electronic mail: munetake.otsuka@grad.nao.ac.jp)

(Dated: 28 October 2024)

The Roberts linkage is recognized for enabling long-period pendulum motion in a compact format. Utilizing this characteristic, we are developing a three-point Roberts linkage for vibration isolation systems, with an eye towards its potential contribution to the development of next-generation interferometric gravitational wave antennas. In this article, we derived the equations to determine the essential parameters when using this linkage as a vibration isolation system, namely the equivalent pendulum length and the relationship between translational motion of the center of mass and rigid body rotation, from size parameters. Additionally, we analyzed the behavior in response to various errors.

I. INTRODUCTION

Interferometric gravitational wave detectors track the space-time distortions reflected in the distance changes between mirrors fixed in an inertial frame, as gravitational waves pass through. Light interference facilitates this precise measurement. Seismic noise, mainly at low frequencies, stands as the major noise source¹, prompting the use of sophisticated vibration isolation systems (VIS) to shield the detectors' test masses from ground vibrations. Enhancing these systems with multiple stages further improves isolation efficiency.

For the multi-stage VIS components, a key requirement is the ability to create a compact, low-frequency pendulum. This is exemplified by devices such as the x-pendulum², the inverted pendulum³, and the Roberts linkage.

In the Einstein Telescope (ET), one of the planned third-generation gravitational wave telescopes, it is necessary to adopt a more advanced vibration isolation system capable of meeting the sensitivity requirements starting from the 0.1 Hz frequency range. Currently, there is a concept to use a low-frequency vibration isolation system based on an inverted pendulum (IP), connecting two stages in series for isolation starting from the 0.1 Hz range.

However, to address the challenge of independently tuning each stage when stacking two IPs, the development of a different type of low-frequency vibration isolation system is needed. The Roberts linkage (RL) has the potential to solve this issue, and a four-point RL has been studied in this context⁴⁻⁷.

The three-point RL⁸, as depicted in FIG. 1, is distinguished by:

- Its ability, similar to four-point RL, to maintain near-horizontal center of mass (COM) movements allows for fine-tuning of the resonance frequency through minor adjustments to the COM position. With a well-designed, concave operational plane, it enables a compact, long-period pendulum with minimal material property impact, relying solely on its geometric design for performance.
- In setups with more than three suspension wires, typi-

cally only three actively support the rigid body at any given moment. As the pendulum moves, the supporting wires may shift, leading to nonlinear behavior and instability. In contrast, the three-point Roberts linkage avoids over-constraining by ensuring that all suspension wires remain consistently engaged, providing stable and reliable operation.

Therefore, it is essential to theoretically investigate the characteristics required for the design and operation of the three-point Roberts linkage.

II. THREE-POINT ROBERTS LINKAGE

This article examines a three-point Roberts linkage (RL) as depicted in FIG. 1. The origin O is placed at the centroid of the 'suspension triangle' $\triangle ABC$, which is an equilateral triangle lying in a horizontal plane, with the x -axis pointing towards 'suspension point' A and the z -axis directed upwards. The suspension points, A , B , and C , all lie in the xy -plane and are positioned at $A(a, 0, 0)$, $B(-a/2, \sqrt{3}a/2, 0)$, and $C(-a/2, -\sqrt{3}a/2, 0)$. Each wire, fixed at one end to the suspension points A , B , and C , has an equal length of $\sqrt{(a/2)^2 + b^2}$, with the other ends attached to points D , E , and F on the rigid body, suspending it. Points D , E , and F form an equilateral triangle on the base of the rigid body, located at a distance of $a/2$ from the central axis, and referred to as the 'fixed points.' The center of mass (COM) of the rigid body is located at point H , which lies on the central axis at a distance of $b + c$ above point G , where the axis intersects the 'base triangle' $\triangle DEF$.

Although counterweights (the gray area in FIG. 1) are attached to the upper part of the rigid body to position the COM at H , and their effects on the COM position, body mass, and moment of inertia are considered, their shape does not directly influence the system's behavior, and thus they are omitted from the subsequent discussion. The wires at both the fixed and suspension points are free to rotate without restriction. In its resting state, with the base triangle parallel to the suspension triangle (the 'horizontal position'), the base triangle is positioned b units below the suspension triangle, and the

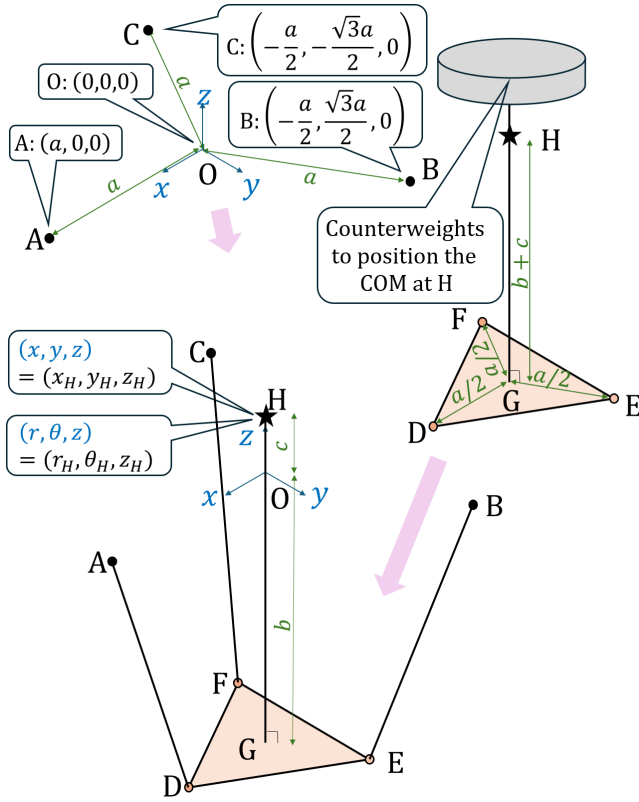


FIG. 1. Three-point Roberts Linkage (RL): The top left image shows the system at rest, along with the coordinate setup. The origin O is at the centroid of an equilateral suspension triangle in the horizontal plane, with suspension points A , B , and C at $(a, 0, 0)$, $(-a/2, \sqrt{3}a/2, 0)$, and $(-a/2, -\sqrt{3}a/2, 0)$, respectively. One end of each wire, with an equal length of $\sqrt{(a/2)^2 + b^2}$, is connected to points A , B , and C , while the other end is connected to points D , E , and F on the rigid body, as shown in the top right image. The rigid body is equipped with counterweights to position the center of mass (COM) at the central axis, at a height of $2b + c$ from the base. The bottom image shows the position where the system is suspended with the base horizontal and at rest. In this position, the center of mass is located at $(0, 0, c)$, and the base of the rigid body lies in the $z = -b$ plane. Both Cartesian coordinates (x_H, y_H, z_H) and cylindrical coordinates (r_H, θ_H, z_H) are used to represent the position of the COM, H .

COM, denoted as H , is located c units above the suspension plane.

When the rigid body is in the horizontal position, the fixed points are defined at $D(a/2, 0, -b)$, $E(-a/4, \sqrt{3}a/4, -b)$, and $F(-a/4, -\sqrt{3}a/4, -b)$, with the COM, H located at $(0, 0, c)$.

The position of the COM, H during operation is given in Cartesian coordinates as (x_H, y_H, z_H) and in cylindrical coordinates as (r_H, θ_H, z_H) .

In this article, we evaluate the behavior of an RL with specific dimensions. We have constructed and are currently evaluating an RL with dimensions $a = 13$ cm, $b = 40$ cm, and $c = 0$ cm. Henceforth, we refer to the RL with these dimensions as the "prototype dimensions" (PD), and this configuration will be denoted as the PDRL (Prototype Dimensions RL) through-

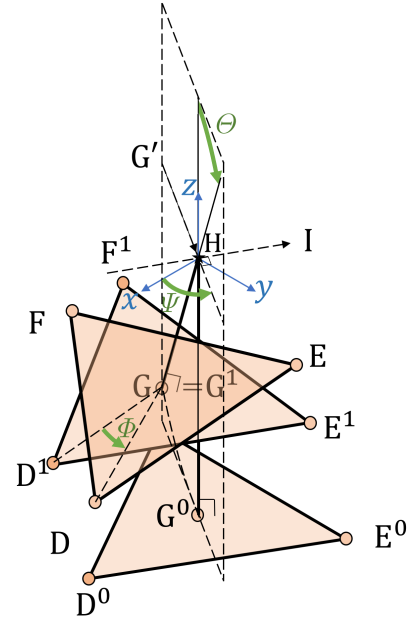


FIG. 2. Definition of Angles: The orientation of the rigid body HDEF is represented by the tilt direction Ψ , tilt angle Θ , and torsion angle Φ . D^0 , E^0 , and F^0 are the positions of D , E , and F when the rigid body is in its nominal rest position with the base triangle horizontal. The angle Ψ is the angle between the projection of the central axis GH onto the x - y plane (denoted as $G'H$) and the x -axis. This angle indicates the direction of tilting but not the rotation angle of the suspension. The tilt angle Θ is the angle between the central axis GH and the z -axis. After the rigid body tilts by Θ in the Ψ direction (rotating around HI by Θ), the corner points shift to D^1 , E^1 , and F^1 . In this tilted position, Φ represents the torsion angle, indicating the rotation around the central axis GH from $D^1E^1F^1$ to DEF .

out the article. Among the PD parameters, c may take values other than 0 cm, but unless otherwise specified, we assume $c = 0$ cm. The behavioral analysis of this prototype has been reported in a separate article⁸.

In this article, the rotational position of the rigid body during the pendulum-like motion of the RL is described using three angles: tilt direction Ψ , tilt angle Θ , and torsion angle Φ . As shown in FIG. 2, the direction in which the rigid body axis GH tilts is represented by the direction Ψ , and the angle Θ . In the coordinate system where the origin is translated to the center of mass H , Ψ is the angle in the xy -plane measured from the x -axis to $G'H$, which is the projection of the vector \vec{GH} onto the xy -plane. The tilt angle Θ is the angle between the rigid body axis GH and the z -axis. In other words, a tilt of direction Ψ and angle Θ is equivalent to a clockwise rotation of Θ around the HI axis, which is at an angle of $\Psi + \pi/2$ from the x -axis in the xy -plane. Φ represents the rotation around the axis GH .

As shown in FIG. 2, a rigid body DEFH with tilt direction Ψ , tilt angle Θ , and torsion angle Φ is the result of rotating the rigid body from its horizontal position $D_0E_0F_0H$, tilted by Θ in the direction Ψ to the position $D_1E_1F_1H$, and then rotating it by Φ around the rigid body axis.

The intended application of the RL discussed in this arti-

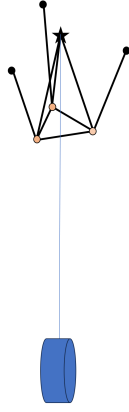


FIG. 3. The Intended Application: The next stage of the VIS, such as a simple pendulum, is expected to be suspended at the COM of the RL.

cle is shown in FIG. 3. We envision incorporating it into the VIS for the test mass in gravitational wave telescopes. As illustrated in the figure, the next stage of the VIS, such as a simple pendulum, is expected to be suspended at the COM of the RL. In the multi-stage vibration isolation system, vibration isolation in the vertical and torsional directions is managed by separate systems, while the RL is responsible solely for isolating horizontal translational motion. The characteristics under this usage can be described by the Lagrangian when the COM moves horizontally relative to the suspension point. Therefore, in the coordinate system where the suspension point is stationary, the RL's characteristics are evaluated by determining the vertical position of the COM, which defines the potential energy, and the rotation of the RL, which defines the kinetic energy, both as functions of the horizontal position of the COM.

III. RIGID BODY MOTION ANALYSIS MODEL

Rigid body motion includes both translational and rotational aspects, featuring six degrees of freedom. For the suspended rigid body, three constraints stipulate that the lengths of the wires AD, BE, and CF are fixed, thereby reducing the available degrees of freedom to three. Consequently, even when the horizontal positions of the center of mass (COM), namely x_H and y_H , are specified, one degree of freedom remains, leaving the height z_H undetermined. This remaining degree of freedom is associated with the torsion angle Φ , which will be discussed further using FIG. 4. Due to this degree of freedom, z_H can vary, and under certain conditions, it can reach a minimal value. Thus, during normal operation of the linkage, it is assumed that this minimum value is achieved. The basis for this assumption in the evaluation of vibration isolation system behavior is discussed further in the 'Discussion' section.

Previous studies⁹ have utilized the method of Lagrange multipliers to find the minimum value of z_H . In contrast, this article employs a geometric approach to this determination.

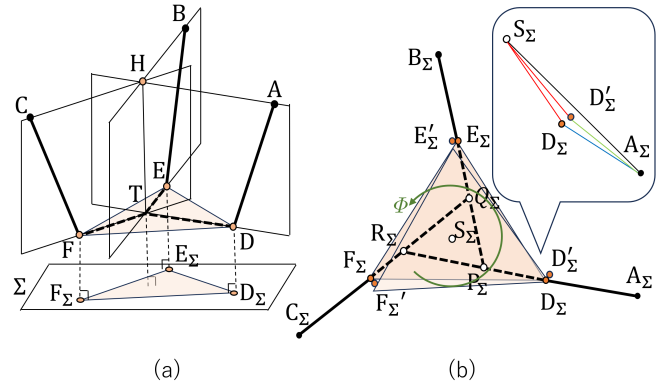


FIG. 4. Constraints for Minimizing z_H Under Fixed x_H and y_H : Panel (a) shows the configuration where the three planes, each formed by one of the three wires and the COM, H, intersect along a single line HT, achieving the minimum z_H . Panel (b) illustrates that the three planes do not intersect along a line but converge at a single point H, forming a triangular pyramid HPQR. This configuration is projected onto plane Σ . Here, a minor rotation from DEF to D'E'F' around the axis HS, as indicated in (b), allows the wires to slacken, which can lower the body's position, thus demonstrating that (b) does not achieve the minimum z_H position.

Geometrically, the constraint for achieving the minimum z_H requires that the three planes, each formed by one of the wires and the COM, H, converge along a single line HT, as depicted in FIG. 4(a). Conversely, when the three planes do not intersect along a single line and instead converge at a single point, H, they form a triangular pyramid HPQR along with the base face DEF of the rigid body. This pyramid is then projected onto a plane Σ , which is perpendicular to the rotational axis HS, with S being a point within triangle PQR. This projection is depicted in panel (b), as indicated by the subscript Σ , which denotes projections onto the Σ plane. From the torque-experiencing configuration of the suspended DEF, it can be inferred that a minor torsion-like rotation of the rigid body from DEF to D'E'F' around the axis HS, centered at S_Σ in (b), permits the wires to slacken, thereby lowering the body's position. In contrast, the configuration illustrated in (a) does not allow any minor rotation that would result in a lower position, thus confirming it as the minimal value of z_H .

Imposing this constraint, along with the three constraints for constant wire lengths, limits the degrees of freedom of the suspended rigid body to two. Therefore, by specifying the horizontal positions x_H and y_H of the COM, the position and orientation of the rigid body are uniquely determined.

Given these constraints, general analytical solutions are challenging to derive, requiring the use of numerical methods for practical resolution. This study employs Newton's method to find numerical solutions, which are outlined as follows:

- Variables (12 in total): These include the positions of four points on the rigid body (x_D, y_D, z_D), (x_E, y_E, z_E), (x_F, y_F, z_F), and (x_H, y_H, z_H).
- Constraints (10 in total):
 - Constant distances for AD, BE, and CF (3 con-

straints),

- Intersection of planes ADH, BEH, and CFH along a single line (1 constraint),
- Constant distances for DE, EF, and FD (3 constraints),
- Constant distances for HD, HE, and HF (3 constraints).

By imposing these constraints, the positions of the four points are calculated as functions of x_H and y_H , allowing for the determination of z_H , Ψ , Θ , and Φ as functions of either (x_H, y_H) or (r_H, θ_H) . Calculations were performed using Mathematica's FindRoot function with 64-digit precision.

IV. ESSENTIAL PARAMETERS FOR VIS AND DERIVATION OF FORMULAS FOR THESE

The goal of this chapter is to derive formulas for calculating essential parameters for RL when utilized as a Vibration Isolation System (VIS), based on its size parameters. Initially, Section A outlines the parameters necessary for determining equivalent pendulum lengths and assessing the contributions of the rigid body's moment of inertia, which are crucial for its effectiveness as a VIS. Ideally, if one could analytically determine the position and orientation of the rigid body from specified size parameters and the horizontal position of the COM, these parameters would be straightforwardly defined. However, this is challenging in practice. Consequently, this article initially focuses on two special cases to facilitate a deeper understanding of the system's behavior. In Section B, we present analytical solutions for the operation of RL along its plane of symmetry for arbitrary sizes. Section C details the numerical analysis of a PDRL, exploring its behavior in various directions. Building upon these findings, Section D formulates hypotheses concerning the behavior of RL in arbitrary directions and sizes, and verifies these hypotheses across different dimensions to validate the general applicability of the derived solutions.

A. Essential Parameters for Motion Analysis

To perform the motion analysis required for utilizing the Roberts linkage (RL) as a horizontal vibration isolation system in gravitational wave telescopes, it is sufficient to describe the potential and kinetic energy in the neighborhood of the stable equilibrium position, where the COM in the horizontal position (x_H, y_H) is close to $(0, 0)$. The potential energy can be determined if the height of the COM, z_H , in the vicinity of $(x_H, y_H) = (0, 0)$ is known, which makes the Hessian matrix in this neighborhood essential for deriving the equations of motion.

The rotation of the rigid body can be described by rotations in the Θ and Φ directions, assuming Ψ is known. If $d\Theta/dr_H$ and $d\Phi/dr_H$ are provided as the body approaches $r_H \rightarrow 0$, the angular velocities in the Θ - and Φ -directions can be derived as

functions of \dot{x}_H and \dot{y}_H , and consequently, the kinetic energy can also be expressed as a function of \dot{x}_H and \dot{y}_H .

In this chapter, we will derive four types of parameters—the Hessian matrix of z_H with respect to x_H and y_H , Ψ , $d\Theta/dr_H$, and $d\Phi/dr_H$ —specifically focusing on those in the vicinity of the stable equilibrium point. Understanding these parameters enables us to construct the Lagrangian of the system based on the horizontal position and horizontal velocity of the COM near the equilibrium point, thereby facilitating the analysis of its dynamics.

B. 2D Motion Analysis Along the Symmetry Plane of the RL

The RL depicted in FIG. 1 is symmetric with respect to the x-z plane. When the COM, H, moves along $\theta_H = 0$, meaning along the symmetry plane, it maintains symmetry which prevents any twisting and causes the rigid body to tilt along the x-axis, thus,

$$\Psi = \Phi = 0. \quad (1)$$

Consequently, when the RL is projected onto the x-z plane as illustrated in FIG. 5, the suspension points B and C, and the fixed points E and F coincide at the same points. The dynamics of the COM (x_H, z_H) and the tilt angle Θ of the rigid body are represented by a two-dimensional RL marked with a red line in the figure, which can be fully described.

When projected onto the x-z plane, points E and F coincide and are both referred to as point E. Describing the system's motion in terms of coordinates (x_E, z_E) for point E, and (x_D, z_D) for point D, the constraints are expressed by three equations corresponding to the constant lengths of line segments AD, BE, and ED. Using these three equations to eliminate three variables, and treating H's position specifically as (x_H, y_H) , we can derive x_H , y_H , z_E , x_D , and z_D as functions solely dependent on x_E . The expressions of x_H , z_H , and $\Theta = (z_E - z_D)/(x_D - x_E)$, as functions of x_E are all quite complex. However, from the equations:

$$\frac{d^2 z_H}{dx_H^2} = \frac{d}{dx_E} \left(\frac{dz_H/dx_H}{dx_E/dx_E} \right) / \frac{dx_H}{dx_E} \quad (2)$$

$$\frac{d\Theta}{dx_H} = \frac{d}{dx_E} \left(\frac{z_E - z_D}{x_D - x_E} \right) / \frac{dx_H}{dx_E} \quad (3)$$

the expressions for $d^2 z/dx_H^2$ and $d\Theta/dx_H$ when $x_H = 0$, that is, when $x_E = -a/4$, are represented by much simpler formulas. Utilizing Mathematica, the following results were obtained.

$$\left. \frac{d^2 z_H}{dx_H^2} \right|_{x_H=0} = \frac{a^2 - 4bc}{4b(2b+c)^2} \quad (4)$$

$$\left. \frac{d\Theta}{dx_H} \right|_{x_H=0} = \frac{1}{2b+c} \quad (5)$$

From Eq. (4), when

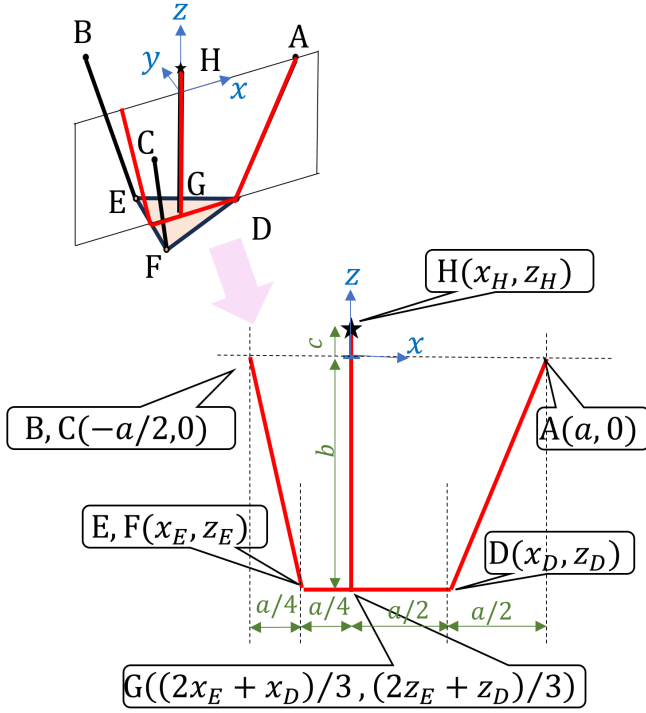


FIG. 5. 2D Analysis: This figure demonstrates that the system can be analyzed in 2D by projecting the COM, H, motion onto the x - z plane. The top left image shows the system as the H moves along the x - z plane, while the bottom right image represents the projection of this system onto the defined plane. The coordinates on this plane are as indicated, facilitating the 2D analysis.

$$c = \frac{a^2}{4b} \equiv c_0, \quad (6)$$

$d^2z/dx_H^2|_{x_H=0}$ becomes 0.

C. 3D Numerical Motion Analysis of the PDRL

In this section, we evaluate the behavior of the RL with the prototype dimensions (PD) parameters, where $a = 13$ cm, $b = 40$ cm and $c = 0$ cm, as described earlier. The RL with these dimensions is referred to as the PDRL (Prototype Dimensions RL). The parameter c is set to 0 cm unless otherwise specified. Specifically, we numerically analyze the behavior of the center of mass height z_H , tilt direction Ψ , tilt angle Θ , and torsion angle Φ as functions of the horizontal position of the center of mass. Particular attention is given to the behavior near the stable point $(x_H, y_H) = (0 \text{ cm}, 0 \text{ cm})$ of the essential parameter discussed in Section A. Moreover, since the behavior of z_H alone is not straightforward when varying the size parameter c , we also evaluate the case where c takes a value other than 0 cm.

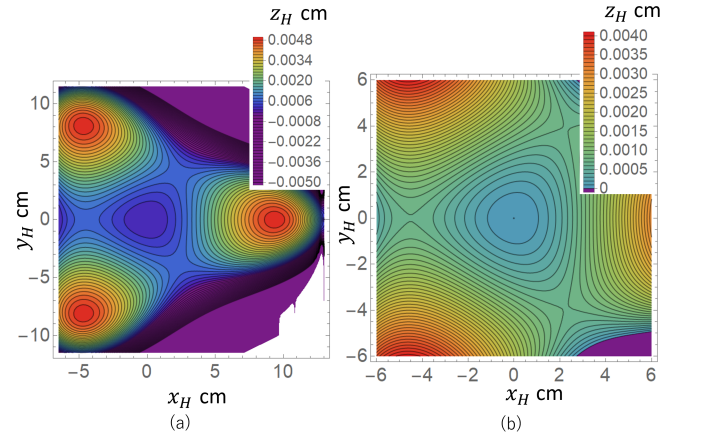


FIG. 6. Contour Maps of the COM's Height: This figure illustrates how the COM's height, z_H , varies relative to its horizontal position (x_H, y_H) in the PDRL. Panel (a) provides a broad view of the behavior, while panel (b) focuses on the central region. Despite the adjustments, changes in z_H are minimal, approximately 0.005 cm, indicating nearly horizontal motion. The contour lines exhibit three-fold symmetry at larger scales but transition to concentric circles, demonstrating isotropy near the center.

1. Center of Mass Height z_H

FIG. 6 depicts the behavior of the COM's height z_H as a function of its horizontal position (x_H, y_H) for the PDRL when $c = 0$ cm. Cross-sectional views for various directions θ_H of the COM are presented in FIG. 7(a). Furthermore, FIG. 7(b) shows d^2z_H/dr_H^2 , the second derivative of z_H , which directly relates to the device's natural frequency. As θ_H approaches zero, d^2z_H/dr_H^2 converges to a constant value, irrespective of θ_H . This value, 0.000165 cm^{-1} , aligns with the calculation $a^2/16b^3$ presented in the previous section's formula (4). The equivalent pendulum length is the reciprocal of this, approximately 6060 cm. In other words, a linkage with dimensions of 13 cm \times 40 cm can achieve an equivalent pendulum length of 60 m, resulting in a pendulum with a period of about 15 seconds (ignoring the moment of inertia of the rigid body).

Next, a small perturbation is introduced by setting $c = 0.5$ cm, which is small relative to the scale of $a = 13$ cm and $b = 40$ cm, and the behavior under this condition is shown in FIG. 8. The isotropic region around the minimum value becomes smaller, and the area surrounding the minimum flattens out. As depicted in FIG. 8(c), $d^2z_H/dr_H^2|_{r_H=0}$ decreases uniformly with θ_H as c increases, reaching zero when $c \approx 1.05$ cm. This value, calculated as $a^2/4b \approx 1.05$ cm, is consistent with the formula (6) derived in the previous section.

The analysis confirms that, specifically in this case, the second derivative of z_H with respect to r_H at $r_H = 0$ remains constant for any value of θ_H , consistent with the value calculated in Equation (4) from the previous section.

$$\left. \frac{d^2z_H}{dr_H^2} \right|_{r_H=0} = \text{constant}, \quad \text{for all } \theta_H. \quad (7)$$

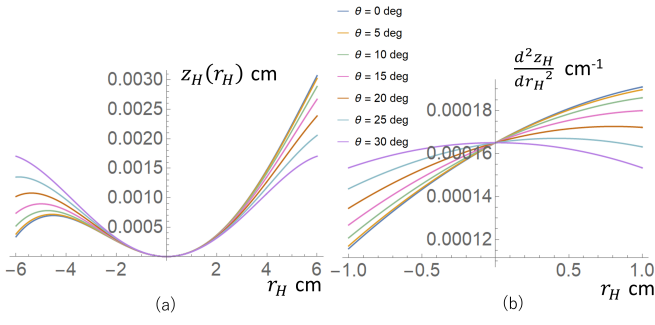


FIG. 7. The COM's Height and Its Second Derivative: Panel (a) of this figure depicts the relationship between the COM's height z_H and radial distance r_H within the range $-6 \text{ cm} \leq r_H \leq 6 \text{ cm}$ for the PDRL, illustrating how z_H varies as a function of r_H at different orientations θ_H . Panel (b) focuses on a closer range $-1 \text{ cm} \leq r_H \leq 1 \text{ cm}$, displaying the second-order derivatives $d^2 z_H / dr_H^2$ as a function of r_H . It emphasizes that these derivatives become isotropic and direction-independent specifically as r_H approaches zero, with a typical value of approximately $1.65 \times 10^{-4} \text{ cm}^{-1}$.

2. Tilt Direction Ψ

The tilt direction Ψ determines the direction in which the system tilts. In other words, it indicates which direction's moment of inertia contributes to the system's kinetic energy. In the PDRL, Ψ is shown as a function of the COM's horizontal position (x_H, y_H) in FIG. 9(a). From the figure, it can be observed that θ_H and Ψ are approximately equal, meaning that the rigid body tends to tilt in the direction of the COM's movement. As discussed in Section B, $\Psi \equiv \theta_H$ holds true for motion along the symmetry plane, such as the $x-z$ plane. To verify this relationship at other angles, the deviation between Ψ and θ_H as a function of $r_H (= \sqrt{x_H^2 + y_H^2})$ is plotted in FIG. 9(b) for various θ_H values. Although $\Psi \neq \theta_H$ for angles other than the symmetry plane ($\theta_H = 0$), the figure confirms that near " $r_H = 0$ ", $\theta_H = 0$, implying that the equation

$$\lim_{r_H \rightarrow 0} \Psi = \theta_H, \quad \text{for all } \theta_H \quad (8)$$

holds.

3. Tilt Angle Θ

The tilt angle Θ represents how much the rigid body tilts in the Ψ direction. In other words, it determines the contribution of the tilt-direction moment of inertia when calculating the kinetic energy from the horizontal movement of the COM. For the PDRL, Θ is shown as a function of the horizontal position of the COM (x_H, y_H) in FIG. 10(a). From the fact that the contour lines are nearly circular and evenly spaced, it can be inferred that Θ is roughly proportional to r_H . As the response to small vibrations near the origin is determined by $d\Theta/dr_H$, as discussed in Section A, we calculate this as a function of r_H for various θ_H values and present it in FIG. 10(b). Although

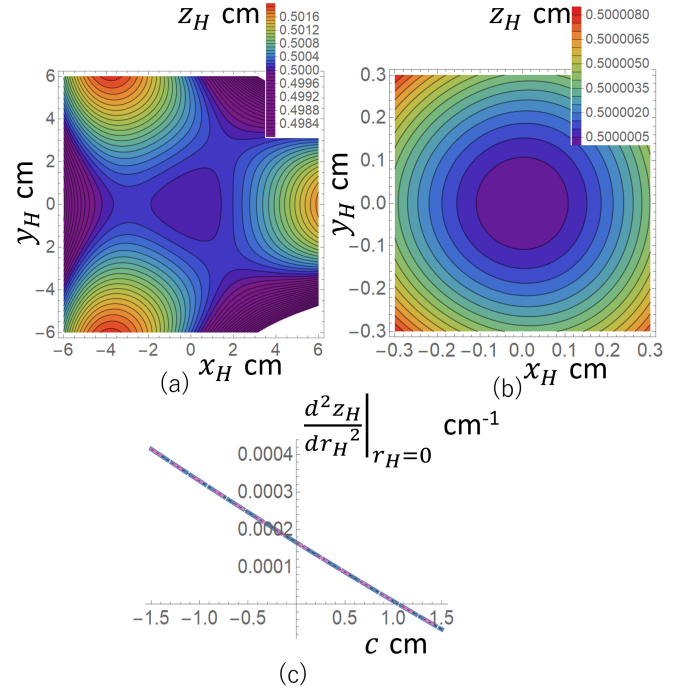


FIG. 8. Behavior of z_H as c Varies in an RL: This figure examines the effects of changing c in a PDRL. Panel (a) shows a contour map of z_H for $c = 0.5 \text{ cm}$, displaying a smaller, shallower central valley at the same scale as FIG. 6(b). Panel (b) zooms into the central region (± 0.3) cm, demonstrating isotropy at $c = 0.5 \text{ cm}$. Panel (c) charts the variations in the second-order derivative $d^2 z_H / dr_H^2$ across different c values, highlighting a consistent decrease to zero at $c \approx 1.05 \text{ cm} \approx a^2/4b$, independent of θ_H .

the shape of the graph changes with different θ_H values, it converges to a single value as r_H approaches zero. That is,

$$\lim_{r_H \rightarrow 0} \frac{d\Theta}{dr_H} = \text{constant}, \quad \text{for all } \theta_H. \quad (9)$$

The constant value 0.0125 cm^{-1} for the PDRL is consistent with Equation (5) in Section B.

4. Torsion Angle Φ

The torsion angle Φ represents the rotation around the rigid body axis. Even when (x_H, y_H) , the horizontal position of the COM, is specified, the RL has a degree of freedom for motion in the Φ direction, allowing various values of Φ . However, as described in Chapter III, this article assumes the value of Φ that minimizes the vertical position of the COM (z_H). Thus, Φ is uniquely determined by (x_H, y_H) , and the analysis is conducted based on this assumption.

For the PDRL, Φ is shown as a function of the center of mass's horizontal position (x_H, y_H) in FIG. 11(a). As mentioned in Section B, for motion along the symmetry planes ($\theta_H = n\pi/3$, n : integer), Φ remains identically zero. However, for other angular directions, it can be observed that not

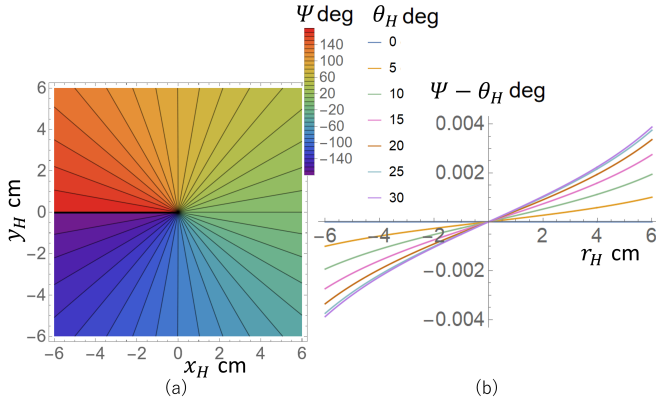


FIG. 9. Behavior of the Tilt Direction Ψ for the PDRL: (a) presents a contour map showing Ψ in relation to the horizontal position of the COM (x_H, y_H) , where $(x_H, y_H) = r_H(\cos \theta_H, \sin \theta_H)$. (b) explores the dependence of Ψ on the radial distance r_H from the origin and its deviation from θ_H for various values of θ_H . It is observed that Ψ closely aligns with θ_H as r_H approaches zero, demonstrating minimal radial displacements.

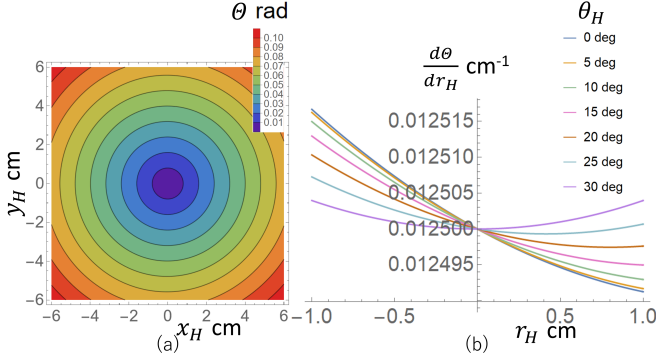


FIG. 10. Behavior of the Tilt Angle Θ for the PDRL: (a) presents a contour map showing Θ in relation to the horizontal position of the COM (x_H, y_H) , where $(x_H, y_H) = r_H(\cos \theta_H, \sin \theta_H)$. (b) explores how $d\Theta/dr_H$, the rate of change of Θ with respect to r_H , varies across different θ_H values. It is noted that $d\Theta/dr_H$ converges to a constant value of 0.0125 cm^{-1} at minimal radial displacements, indicating a significant consistency in tilt behavior as r_H approaches zero.

only tilt Θ but also torsion Φ arises as the center of mass is displaced horizontally. Similarly to Θ , $d\Phi/dr_H$ is calculated as a function of r_H for various values of θ_H , and the results are presented in FIG. 11(b). As the deviation from the symmetry axis increases, $d\Phi/dr_H$ deviates from zero, but even in such cases, as r_H approaches zero, $d\Phi/dr_H$ converges to zero. That is,

$$\lim_{r_H \rightarrow 0} \frac{d\Phi}{dr_H} = 0, \quad \text{for all } \theta_H. \quad (10)$$

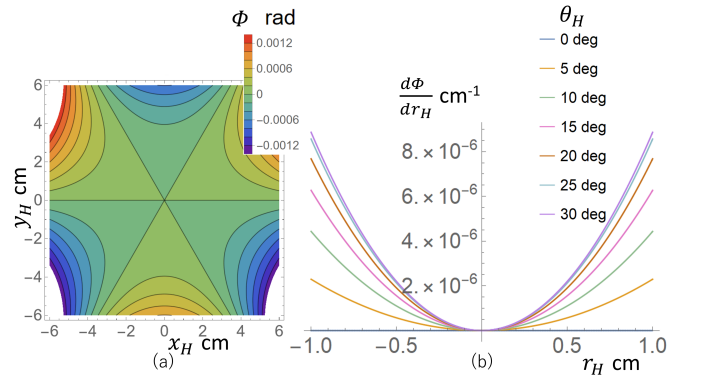


FIG. 11. Behavior of the Torsion Angle Φ for the PDRL: (a) presents a contour map showing Φ relative to the horizontal position of the COM (x_H, y_H) , where $(x_H, y_H) = r_H(\cos \theta_H, \sin \theta_H)$. (b) explores the relationship between the radial distance r_H from the COM and the rate of change $d\Phi/dr_H$ across various θ_H values. It is observed that $d\Phi/dr_H$ tends towards zero as r_H approaches zero.

D. Hypothesis and Verification

Up to this point, our discussion had spanned the analysis of directional behavior for Roberts linkages of arbitrary dimensions and the evaluation of behavior in arbitrary directions for specific-sized RLs. Given the consistent findings and absence of discrepancies between these analyses, we were then poised to formulate hypotheses regarding the behavior of RLs across any dimensions and directions, and proceeded to systematically evaluate these hypotheses.

1. Formulating Hypotheses for RL Behavior

From Equations (4) and (7), it is posited for RLs of any dimension that:

$$\left. \frac{d^2 z_H}{dr_H^2} \right|_{r_H=0} = \frac{a^2 - 4bc}{4b(2b+c)^2}, \quad \text{for all } \theta_H. \quad (11)$$

This can also be expressed using the Hessian matrix as follows:

$$\left(\begin{array}{cc} \frac{\partial^2 z_H}{\partial x_H^2} & \frac{\partial^2 z_H}{\partial x_H \partial y_H} \\ \frac{\partial^2 z_H}{\partial x_H \partial y_H} & \frac{\partial^2 z_H}{\partial y_H^2} \end{array} \right) \Big|_{r_H=0} = \frac{a^2 - 4bc}{4b(2b+c)^2} \begin{pmatrix} 1 & 0 \\ 0 & 1 \end{pmatrix}. \quad (12)$$

Similarly, from Equations (1) and (8), (5) and (9), and (1) and (10), it is presumed for RLs of any dimension that:

$$\lim_{r_H \rightarrow 0} \Psi = \theta_H, \quad \text{for all } \theta_H. \quad (13)$$

$$\lim_{r_H \rightarrow 0} \frac{d\Theta}{dr_H} = \frac{1}{2b+c}, \quad \text{for all } \theta_H. \quad (14)$$

$$\lim_{r_H \rightarrow 0} \frac{d\Phi}{dr_H} = 0, \quad \text{for all } \theta_H. \quad (15)$$

These relationships, expressed as Equations (12) to (15), are posited as hypotheses.

2. Verification of Hypotheses

We conducted numerical verification across various RL dimensions, examining 31 values each for dimensions a and b ranging from 1 to 1000, 11 values for c ranging from 0 up to c_0 as defined in Equation (6), and 7 values for θ_H from 0 to 30 degrees.

For Equation (12), we verified that two eigenvalues of the Hessian matrix remained consistent across all 10,571 ($31 \times 31 \times 11$) combinations of a, b , and c .

Assuming the validity of Equations (13) and (14), the behavior of the system posits that the rigid body rotates about a fixed point located at $(2b+c)$ units directly beneath the COM. Thus, at the same rigid body position with $c=0$, the horizontal position is given by $(2b/2b+c)(x_H, y_H)$. Consequently, if we denote $\Psi(x_H, y_H)$ at $c=0$ as $\Psi_0(x_H, y_H)$, it follows that:

$$\Psi(x_H, y_H) = \Psi_0\left(\frac{2b}{2b+c}x_H, \frac{2b}{2b+c}y_H\right) \quad (16)$$

This implies that if Equation (13) is verified at $c=0$, it is expected to hold for any c . Similarly, if the validity of Equations (14) and (15) is confirmed at $c=0$, they are presumed valid for any c . Therefore, verification of these equations at $c=0$ is sufficient. Accordingly, Equations (13) through (15) were tested at $c=0$ across 6,727 ($31 \times 31 \times 7$) combinations of a, b , and θ_H .

These findings affirm that our hypotheses are universally applicable, rendering them suitable for RLs of any dimension in practical applications.

These findings affirm that Equations (12) to (15) are universally applicable, rendering them suitable for RLs of any dimension in practical applications.

V. INFLUENCE AND COMPENSATION OF STRUCTURAL VARIATIONS

In this chapter, we examined the influence on the COM's gliding plane, represented by $z_H(x_H, y_H)$, when the PDRL was subjected to suspension plane inclination, wire length discrepancies, and horizontal displacement of the COM. The results showed that even small errors significantly affect the rigid body's resting position, and d^2z_H/dx_H^2 and d^2z_H/dy_H^2 changes its value anisotropically. Additionally, these three types of errors can potentially cancel each other out to stabilize the rigid body at the center, but issues of anisotropy may still remain.

1. Effects of Inclination

To investigate the behavior of the PDRL when tilted around the y-axis, we adjusted the position of suspension point A from its original location at $(a, 0, 0)$ to $(a, 0, \epsilon_A)$ and analyzed its behavior. This analysis included examining the shift in the x-coordinate of z_H 's minimum point, denoted as x_{\min} , as illustrated in FIG. 12.

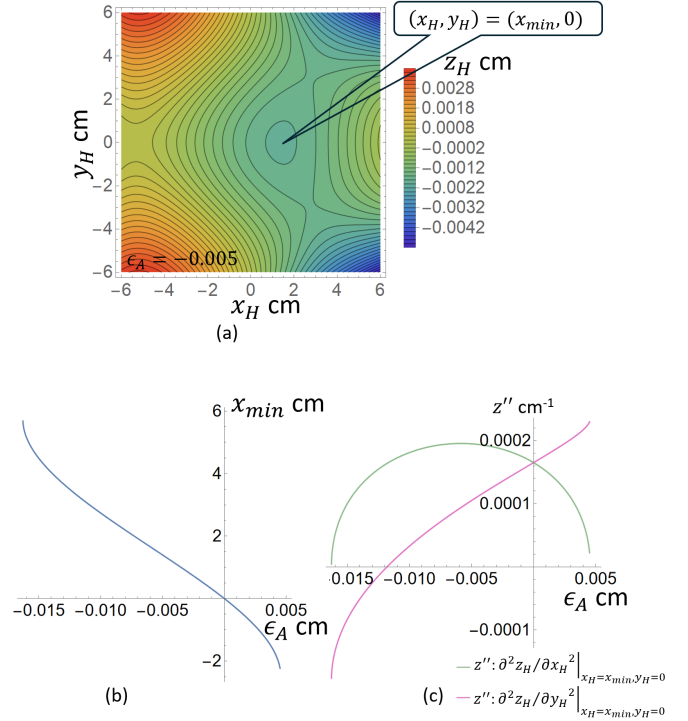


FIG. 12. Effects of a Minor Tilt Around the Y-Axis: This figure explores the effects of tilting on the PDRL by vertically adjusting only suspension point A to positions $(a, 0, \epsilon_A)$. Panel (a) displays contour lines of $z_H(x_H, y_H)$ for $\epsilon_A = -0.005$ cm, illustrating the shift of the z_H 's minimum point along the x-axis and its resulting anisotropic deformation. Panel (b) shows the relationship between ϵ_A and the x-coordinate x_{\min} of z_H 's minimum point. Panel (c) presents how changes in ϵ_A affect the second derivatives $\partial^2 z_H / \partial x_H^2$ and $\partial^2 z_H / \partial y_H^2$ at the minimum point $(x_{\min}, 0)$, highlighting the induced anisotropy in the deformation patterns.

FIG. 12(a) presents the contour lines of $z_H(x_H, y_H)$ when $\epsilon_A = -0.005$ cm, highlighting a shift in the minimum point of z_H along the x-axis and anisotropic deformation around this point.

FIG. 12(b) depicts the relationship between ϵ_A and the x-coordinate of z_H 's minimum point x_{\min} . Lowering point A shifts x_{\min} in the positive x-direction, while raising it shifts x_{\min} in the negative x-direction.

FIG. 12(c) demonstrates how ϵ_A influences the second derivatives $\partial^2 z_H / \partial x_H^2$ and $\partial^2 z_H / \partial y_H^2$, making the behavior around the minimum point non-isotropic. Specifically, when $\epsilon_A < -0.012$ cm, the minimum point becomes a saddle point.

These results are consistent with the gliding plane shown in FIG. 6 after introducing a tilt by ϵ_A , that is, by adding an inclination to $z_H(x_H, y_H)$ in FIG. 6.

2. Effects of Wire Length Discrepancies

This section examines the behavior of the PDRL when there is a slight deviation in one of its wire lengths. Normally, the length of wire AD should be $l \equiv \sqrt{(a/2)^2 + b^2}$; however, we

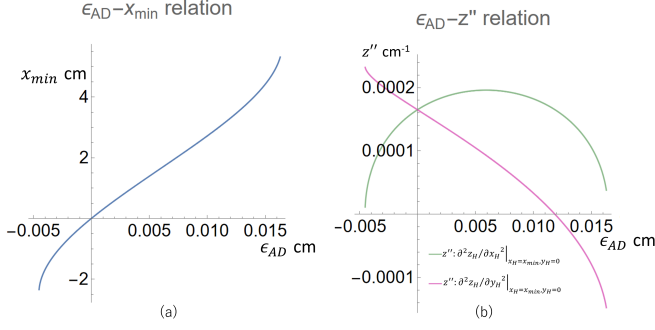


FIG. 13. Effects of Wire Length Discrepancies: Panel (a) depicts the relationship between the wire length change ϵ_{AD} and the x -coordinate of the z_H minimum point, x_{min} . Increasing the length of wire AD shifts the minimum point in the $+x$ direction, while decreasing it shifts the point in the $-x$ direction. Panel (b) illustrates the impact of ϵ_{AD} on the second derivatives $\partial^2 z / \partial x_H^2$ and $\partial^2 z / \partial y_H^2$ at the z_H minimum point, highlighting how changes in wire length affect the curvature of the surface at the minimum point.

consider it to be $l + \epsilon_{AD}$ and analyze the implications of this minor change. The results are presented in FIG. 13.

In FIG. 13, panel (a) shows how a change in ϵ_{AD} affects the position of the minimum z_H , plotting ϵ_{AD} against the x -coordinate x_{min} of the minimum point. Panel (b) demonstrates the relationship between ϵ_{AD} and the second derivatives $\partial^2 z_H / \partial x_H^2$ and $\partial^2 z_H / \partial y_H^2$ at the minimum point.

3. Effects of the COM's Horizontal Displacement

For the PDRL, FIG. 14 shows behavior, in the same manner as FIG. 13, when the COM, normally positioned at $(0, 0, c)$ in a state where the base plane is horizontal, is displaced to $(\epsilon_x, 0, c)$. Panel (a) illustrates the displacement of the minimum point of z_H in response to ϵ_x , plotting the relationship between ϵ_x and the x -coordinate of z_H 's minimum point, x_{min} . Panel (b) displays the relationship between ϵ_x and the second derivatives $\partial^2 z_H / \partial x_H^2$ and $\partial^2 z_H / \partial y_H^2$ at the minimum point of z_H .

Even a slight shift of the COM in the positive x direction results in a substantial corresponding shift of x_{min} in the same direction.

4. Compensation through Wire Length Adjustments

As we have observed so far, inclination ϵ_A , wire length discrepancies ϵ_{AD} , and the COM's horizontal displacement ϵ_x exhibit similar characteristics, which leads to the consideration of canceling them out mutually. Adjusting wire length through heating has been previously studied⁴, and here, we explore the possibility of compensating for the inclination ϵ_A and COM's horizontal displacement ϵ_x by adjusting the wire length ϵ_{AD} . Specifically, for ϵ_A and ϵ_x values of -0.2 cm, 0 cm, and $+0.2$ cm, we determine the ϵ_{AD} that makes the minimum

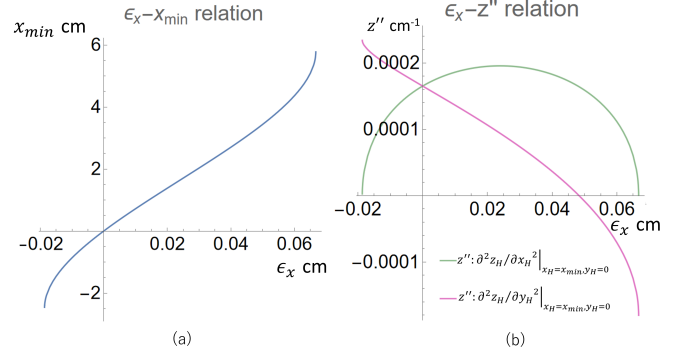


FIG. 14. Effects of COM's Horizontal Displacement: Panel (a) illustrates the relationship between the horizontal displacement of the COM ϵ_x and the x -coordinate of the minimum point of z_H , denoted as x_{min} . A shift of the COM in the $+x$ direction results in a corresponding shift of the minimum point along the $+x$ axis. Panel (b) demonstrates the effects of ϵ_x on the second derivatives $\partial^2 z_H / \partial x_H^2$ and $\partial^2 z_H / \partial y_H^2$ at the minimum point of z_H . It highlights how displacements in the COM influence the anisotropic deformation characteristics around the minimum point.

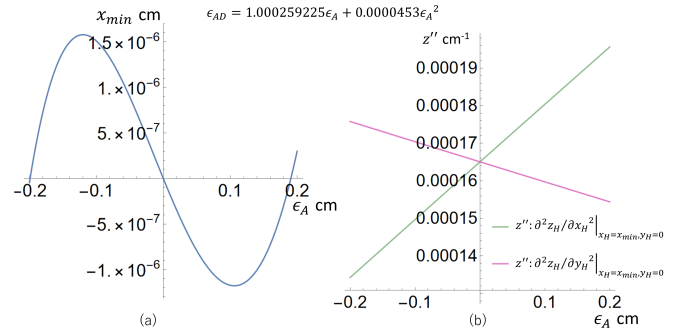


FIG. 15. Adjusting Wire Length to Compensate for Tilt Effects: This figure illustrates how the effects of tilt (ϵ_A) are canceled by small adjustments to the wire length ϵ_{AD} , given by $\epsilon_{AD} = 1.000259225\epsilon_A + 0.0000453\epsilon_A^2$. Panel (a) shows that specific adjustments to ϵ_{AD} can effectively maintain the position of the z_H minimum point within a range of $\pm 2 \times 10^{-6}$ cm, despite variations in ϵ_A . Panel (b) highlights that, although the minimum position can be maintained centrally, the second derivatives $\partial^2 z_H / \partial x_H^2$ and $\partial^2 z_H / \partial y_H^2$ vary, indicating that the shape around the minimum point does not retain isotropy.

point of z_H satisfy $x_H = 0$, placing it on the z -axis. The results of compensating using a quadratic function interpolated between these three points for ϵ_{AD} are shown in FIG.15 and FIG.16. In each figure, the equation shown to determine ϵ_{AD} is the quadratic interpolation function used for compensation. Panel (a) in each figure displays x_{min} after compensation using this interpolation, and in both cases, x_{min} is found to be very small, indicating that the compensation is effective. However, even in such cases, as shown in Panel (b), the values of the second derivatives $\partial^2 z_H / \partial x_H^2$ and $\partial^2 z_H / \partial y_H^2$ diverge, indicating that isotropy cannot be maintained at the minimum point.

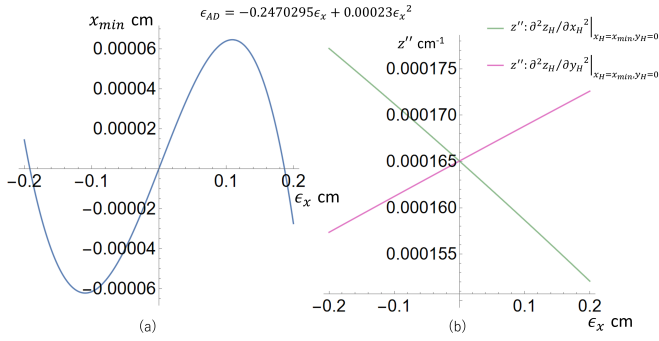


FIG. 16. Adjusting Wire Length to Compensate for COM's Horizontal Displacement: This figure illustrates how the effects of COM's Horizontal Displacement (ϵ_x) are canceled by small adjustments to the wire length ϵ_{AD} , given by $\epsilon_{AD} = -0.2470295\epsilon_x + 0.00023\epsilon_x^2$. Panel (a) shows that appropriate adjustments to ϵ_{AD} can effectively maintain the position of the z_H minimum point within a range of $\pm 6 \times 10^{-5}$ cm, despite variations in ϵ_x . Panel (b) highlights that, although the minimum position can be maintained centrally, the second derivatives $\partial^2 z_H / \partial x_H^2$ and $\partial^2 z_H / \partial y_H^2$ vary independently, indicating that the shape around the minimum point does not retain isotropy.

VI. DISCUSSION

The discussions so far have proceeded on the premise that the minimum possible value of z_H is considered for given horizontal positions x_H, y_H of the COM. However, the rigid body also has a degree of freedom in torsion Φ , and its position is defined within this three-dimensional phase space.

Nevertheless, when used as a vibration isolation system (VIS) for gravitational wave detectors, the following considerations apply:

- The system is typically operated very close to the most stable equilibrium point, $x_H = 0, y_H = 0, \Phi = 0$.
- The motion that requires isolation is translational, and no external forces are applied that would induce rotational motion in the Φ direction.
- According to Equation (15), minimal motions in the x_H, y_H directions do not induce rotations in Φ , as $\Phi = 0$ corresponds to the position of the lowest COM and the minimum potential energy.

Considering these factors, the premise that z_H attains its minimum value as described in this article is justified and sufficient for practical purposes.

The three-point RL exhibits isotropy at infinitesimal amplitudes, and its equivalent pendulum length r_0 is given by

$$r_0 = \frac{1}{d^2 z_H / dr_H^2} = \frac{4b(2b+c)^2}{a^2 - 4bc}. \quad (17)$$

At $c = 0$, r_0 becomes $16b^3/a^2$, which implies that it scales with dimension in similar shapes. However, when the lateral dimension a is constant, r_0 is proportional to the cube of b , and it's easy to extend the equivalent pendulum length by adjusting c .

As $\Psi \rightarrow \theta$ when $r \rightarrow 0$, it can be considered that the direction in which the axis tilts during infinitesimal amplitude oscillations is the same as the direction of these oscillations. The rotational motion determined by this tilting is governed by the moment of inertia, which can be assessed from the COM oscillation by

$$\frac{d\Theta}{dr_H} = \frac{1}{2b+c}. \quad (18)$$

There's no need to consider torsion around the rigid body axis.

This article presents a theoretical examination under the assumption that there is no deformation of the rigid body or extension and vibration of the wires. Therefore, in actual devices where such effects cannot be neglected due to the material properties, mass, and dimensions of the device, including the wire, it is necessary to consider appropriate corrections. In practice, it is assumed that the linkage is constructed by clamping both ends of the wire to the support and the rigid body, with the wire bending at the clamp points. The impact of wire extension becomes more significant as the wire diameter decreases. On the other hand, as the wire becomes thicker, the displacement of the pivot point increases, requiring careful attention.

VII. CONCLUSION

This study elucidated the equivalent pendulum length necessary for using the three-point RL as a VIS, as well as the rigid body rotation corresponding to oscillations. The influence of structural variations were also clarified.

In the future, key theoretical challenges will include addressing wire elongation and flexure correction. On the implementation side, the development of methods to correct and control the sensitive parameters identified in this study will be a critical focus.

ACKNOWLEDGMENTS

This research was supported by International Graduate Program for Excellence in Earth-Space Science (IGPEES), a World-leading Innovative Graduate Study (WINGS) Program, the University of Tokyo.

¹Y. Michimura, K. Komori, Y. Enomoto, K. Nagano, A. Nishizawa, E. Hirose, M. Leonardi, E. Capocasa, N. Aritomi, Y. Zhao, R. Flaminio, T. Ushiba, T. Yamada, L. Wei, H. Takeda, S. Tanioka, M. Ando, K. Yamamoto, K. Hayama, S. Haino, and K. Somiya, "Prospects for improving the sensitivity of the cryogenic gravitational wave detector KAGRA," *Phys. Rev. D* **102**, 022008(10) (2020).

²M. Barton and K. Kuroda, "Ultralow frequency oscillator using a pendulum with crossed suspension wires," *Rev. Sci. Instrum.* **65**, 3775–3779 (1994).

³A. Takamori, P. Raffai, S. Marka, R. DeSalvo, V. Sannibale, H. Tariq, A. Bertolini, G. Cella, N. Viboud, K. Numata, R. Takahashi, and M. Fukushima, "Inverted pendulum as low-frequency pre-isolation for advanced gravitational wave detectors," *Nucl. Instrum. Methods Phys. Res. A* **582**, 683–692 (2007).

⁴J. Dumas, P. Barriga, C. Zhao, L. Ju, and D. Blair, "Compact vibration isolation and suspension for australian international gravitational observatory: Local control system," *Rev. Sci. Instrum.* **80**, 114502 (2009).

- ⁵F. Garoi, J. Winterflood, L. Ju, J. Jacob, and D. G. Blair, “Stability of non-linear modes,” *Rev. Sci. Instrum.* **74**, 3487–3491 (2003).
- ⁶J. Dumas, L. Ju, and D. Blair, “Modelling of tuning of an ultra low frequency roberts linkage vibration isolator,” *Phys. Lett. A* **374**, 3705–3709 (2010).
- ⁷R. Takahashi and K. Mitsuhashi, “Hybrid low frequency seismic isolation system for the 3rd generation gravitational wave detectors,” (2023).
- ⁸K. Mitsuhashi, “Development of two-stage low-frequency vibration isolation system using roberts linkage suspended by 3 wires and inverted pendulum,” Master’s thesis, the University of Tokyo (in Japanese) (2024).
- ⁹P. Bosetti, F. Biral, and D. Bortoluzzi, “Design, manufacturing, and performance verification of a Roberts linkage for inertial isolation,” *Precision Engineering* **38**, 138–147 (2014).